Asymmetric oxygen vacancy-enriched Mn_2O_3@CeO_2 for NO oxidation with excellent low-temperature activity and boosted SO_2-resistance

Lei Chen [a], Dan Ren [a], Xiaoke Hou [a], Jinping Zhang [b], Yangwen Wu [c], Yibio Wang [a], Chao Hu [a], Peigao Duan [a,*], Chao Li [d], Ching-Yu Chiang [e], Chi He [b,*], Qiang Lu [c,*]

[a] School of Chemical Engineering and Technology, Xi'an Jiaotong University, Xi'an, Shaanxi 710049, China
[b] State Key Laboratory of Multiphase Flow in Power Engineering, Xi'an Jiaotong University, Xi'an, China
[c] National Engineering Research Center of New Energy Power Generation, North China Electric Power University, Beijing 102206, China
[d] Instrument Analysis Center of Xi'an Jiaotong University, Xi'an Jiaotong University, No. 28 West Xianning Road, Xi'an 710049, China
[e] National Synchrotron Radiation Research Center, Hsinchu 30076, Taiwan, ROC

ARTICLE INFO

ABSTRACT

The development of highly active and SO_2-resistant catalysts is a major hurdle in the catalytic oxidation of NO to NO_2. Herein, we fabricate a core–shell Mn_2O_3@CeO_2 catalyst using a two-step method for NO oxidation. Benefiting from the generation of abundant Mn^{4+}–O_v–Ce^{3+} interfacial sites and plentiful oxygen vacancies, the resulting Mn_2O_3@CeO_2 exhibits a superior low-temperature NO-to-NO_2 capacity (T_{50} at 183 °C and T_{86} at 275 °C), obtaining a remarkable temperature reduction compared to commercial Pt/γ-Al_2O_3 catalyst (T_{50} at 262 °C). Meanwhile, *In-situ* Raman and *In-situ* Drifts reveal that Mn^{4+}–O_v–Ce^{3+} interfacial site is the main adsorption site for the formation of N-containing intermediates, which plays a decisive role in the NO oxidation reaction. More encouragingly, SO_2 shows a much higher affinity for CeO_2 sheath (E_{CeO_2,SO_2} = –3.48 eV) than Mn_2O_3 core ($E_{Mn_2O_3,SO_2}$ = –0.87 eV), thus avoiding its toxic effects on the interior active sites and endowing Mn_2O_3@CeO_2 a superior SO_2-resistance.

1. Introduction

Coal-combustion related industrial activities contribute greatly to global economic development and energy security, accompanied by the discharge of large amounts of anthropogenic contaminants. The efficient elimination of NO_x from the coal combustion process has become increasingly urgent due to the stringent requirements of current ultra-low emission reformation. As a sustainable alternative, catalytic oxidation of NO to NO_2 is considered to be the crucial step for various terminal treatment approaches, including lean NO_x trap and NO_x selective catalytic reduction [1–3]. The core of this technology banks on exploiting high-performance catalysts. Although platinum group metals such as Pt [4], Pd [5], and Ru [6] loaded materials (PGMs) have exhibited satisfactory activity, extreme scarcity, and high cost hinder their massive production and wide applications. In past years, much effort has been paid attention to exploiting good-performing and low-cost transition metal oxide (TMO) catalysts; however, their performance cannot match that of PGMs. To address this, the development of economical NO oxidation catalysts with excellent low-temperature activity and good stability is highly desirable.

Recently, MnO_x–CeO_2 ternary composites with multiple valences and strong oxygen storage capacity have shown wonderful performance in a series of redox reactions, including selective oxidation of hydrocarbons [7], CO oxidation [8], fast selective catalytic reduction, and volatile organic compound combustion [9]. Compare with the pure MnO_x and CeO_2, the significant improvement of catalytic performance empowered by MnO_x–CeO_2 hybrid catalyst is very attractive, which is typically ascribed to synergistic effects between the two counterparts with enhanced reducibility [10]. The vital role of the manganese–cerium interface in MnO_x–CeO_2 hybrid oxides in catalysis has been well verified, and defined as $Mn_xCe_{1-x}O_y$ solid solution [11]. Based on this theory, various strategies, such as sol-gel [12], impregnation [13], coprecipitation [14], hydrothermal [15], and combustion methods [16], have been employed to prepare MnO_x–CeO_2 composite. Nevertheless, traditional preparation methods often are accompanied by the generation of multiphase, which overshadows the understanding on the chemical nature of intrinsic active sites at the manganese–cerium interfacial perimeter. Additionally, previous literature often mistakes

increased oxygen vacancy concentrations as the core in promoting catalytic activity for redox reaction. In fact, the effect of defect sites (O vacancies; metastable cations) in mixed oxides is also highly dependent on the chemical environment of the active sites (bonding strength, site symmetry, interaction between defects, etc.) [10]. Very recently, Yu et al. [17] pointed out that the coordination environment of oxygen vacancy plays a crucial role in its catalytic performance. As compared to the symmetrical oxygen vacancy, the asymmetrical oxygen vacancy shows a stronger superiority of absorbing the reactive intermediates and desorbing the resultant products, benefiting molecules' easy capture and escape (Scheme 1a). For instance, Shen and his co-workers found that $Cu^+–O_v–Ce^{3+}$ in Cu/CeO_2 catalyst serve as active sites for the water–gas shift reaction, and these sites exhibit a cooperative effect during the reaction with the $O_v–Ce^{3+}$ sites dissociatively activating H_2O and the Cu^+ sites adsorbing CO [18]. Also, Tang et al. [19] reported that transition metal (M = Fe, Co, and Ni) doping into the CeO_2 lattice could form asymmetric oxygen vacancies ($M–O_v–Ce$) and accelerate the COS hydrolysis rate. Recently, Lee et al. [20] proposed that the well-defined heterointerface of the fluorite CeO_2 and the bixbyite Y_2O_3 provided an excellent platform for the generation of asymmetric oxygen vacancies. With the merits of low prices and abundant mineral reserves, Mn_2O_3 and CeO_2-based materials exhibit significant research potential in various industrial sectors, such as energy storage [21], catalysis [22], and environmental remediation [23]. In the fluorite-type CeO_2 and bixbyite-type Mn_2O_3, the oxygen anions are tetrahedrally coordinated by four cations. Given the superiority of CeO_2 and Mn_2O_3 structure, the combination of these two components seems a wise choice to enhance the redox abilities, because the asymmetric "$Mn–O_v–Ce$" site formed in this hybrid composite is more reactive in redox reactions than symmetric "$Mn–O_v–Mn$" or "$Ce–O_v–Ce$" sites. Further investigation is required for a comprehensive understanding of the functionality of these asymmetric sites in catalytic oxidation reactions.

Inspired by the above-mentioned backgrounds, we synthesized a core-shell Mn_2O_3 @CeO_2 catalyst (Scheme 1b) using a hydrothermal technique, with the objective to provide a high-performance NO oxidation catalyst to substitute the current commercial Pt/γ-Al_2O_3 catalyst. As a result, the prepared catalyst exhibits excellent low-temperature catalytic activity in NO oxidation (T_{50} at 183 °C and T_{86} at 275 °C), which is significantly superior to the Pt/γ-Al_2O_3 catalyst (T_{50} at 320 °C). Characterization uncover that an asymmetric coordination of manganese–cerium interfacial perimeter can effectively promote the formation of N-containing intermediates, which is regarded as the rate-determining step for the whole NO oxidation reaction. Furthermore, the CeO_2 sheath can significantly improve the antipoisoning ability of prepared Mn_2O_3 @CeO_2 material, endowing it a strong SO_2-tolerance and good cycling stability.

2. Experimental

2.1. Catalyst preparation

Mn_2O_3 @CeO_2 cube was synthesized by two steps: 1) Synthesis of Mn_2O_3 cubes [24]. 1 mmol $KMnO_4$ was slowly added into a 60 mL solution containing a stoichiometric amount of glucose (0.3 mmol) and stirred for 30 min, and then transferred to the 100 mL Teflon-lined stainless autoclave for hydrothermal treatment at 160 °C for 4 h. After cooling down to the room temperature, the resultant precipitate was washed with ethanol and deionized water for several times. The dried solid was calcined in air at 550 °C for 2 h, yielding Mn_2O_3 cubes. 2) Synthesis of Mn_2O_3 @CeO_2 cubes [25]. 0.1 g as-obtained Mn_2O_3 cubes were added to a 60 mL ethanol and sonicated for 2 h. Then, a 40 mL mixed solution of hexamethylenetetramine (0.04 g) and $Ce(NO_3)_3$ (0.02 g) was dropwise added into the above solution and heated at 75 °C for 2 h. Finally, the resulting precipitate was ethanol and deionized
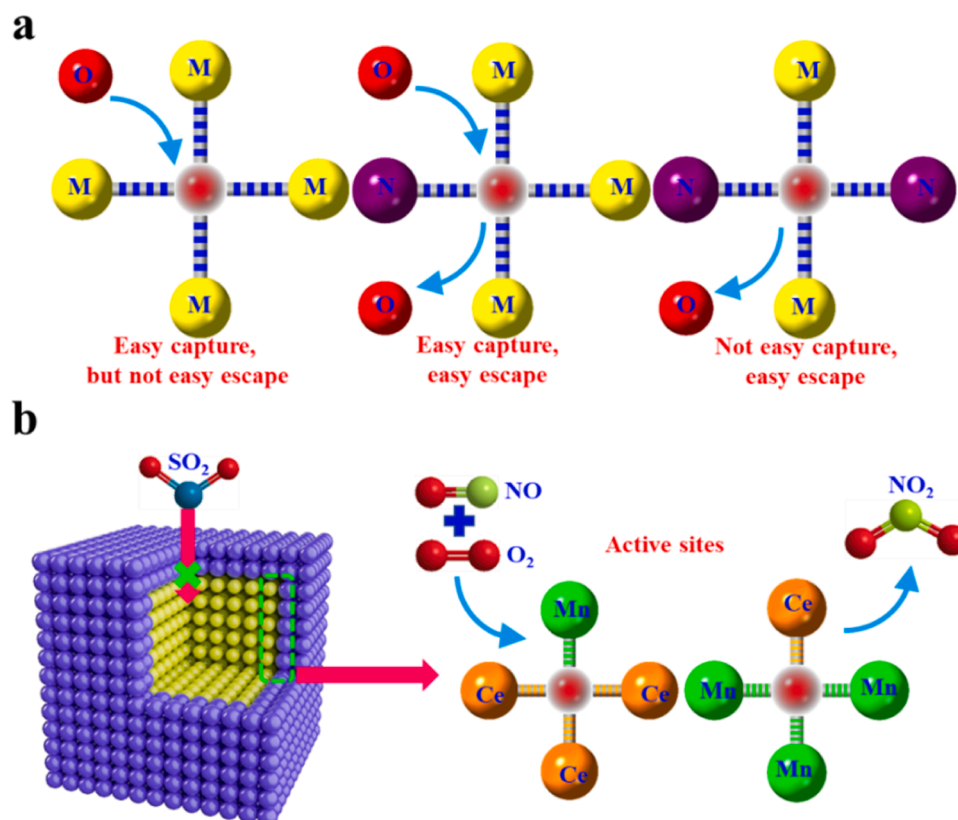
Scheme 1. . (a) The relationships between local environment of oxygen vacancy and its redox property[17]; (b) Schematic diagram of asymmetric oxygen vacancy-enriched Mn_2O_3 @CeO_2.

water for several times, and then calcined in air at 400 °C for 1 h.

2.2. Catalyst characterizations

The synthesized catalysts were characterized using various techniques, including X-ray diffraction (XRD), X-Ray Fluorescence (XRF), nitrogen adsorption–desorption, scanning electron microscopy (SEM), transmission electron microscopy (TEM), X-ray photoelectron spectroscope (XPS), Raman spectroscopy, hydrogen temperature-programmed reduction (H$_2$-TPR), oxygen temperature-programmed desorption (O$_2$-TPD), low-temperature solid-state electron paramagnetic resonance (EPR), electron energy loss spectroscopy (EELS), in-situ Raman and in-situ DRIFTS. Detailed information about the instruments and their operating conditions are provided in the Supplementary Information.

2.3. Catalytic evaluation

The NO oxidation reactions were carried out on a fixed-bed reactor ($\Phi = 6.0$ mm) at atmospheric pressure. 0.2 mL catalysts were used to investigate the NO oxidation reaction, with the following reaction parameters: 500 ppm of NO, 10 vol% O$_2$, 100–300 ppm of SO$_2$ (when used), and 5 vol% H$_2$O (when used). The balance gas was N$_2$ with a total flow rate of 300 mL·min^{-1}, and the corresponding reaction gas hourly space velocity (GHSV) was 90,000 h^{-1}. The compositions of effluent gases were monitored online using a Gasmet DX4000 FTIR gas analyzer, and the NO conversion efficiency was defined as follows:

$$X_{\mathrm{NO}} = \frac{(C_{in} - C_{out})}{C_{in}} \times 100\% \tag{1}$$

Kinetic measurements were performed to evaluate the activation energy of prepared materials. A mixture of catalysts (50 mg) and inert silica pellets (450 mg) was employed in each experiment. The study of NO oxidation kinetics was conducted using the same gas composition employed in the oxidation reaction above, with the only difference being that the GHSV was increased to 300,000 h^{-1}. Despite this, the conversion of NO to NO$_2$ was less than 20 %. Data were only collected after the catalyst had been on stream for at least an hour, and a steady state had been attained. The apparent activation energy (E_a) was then calculated based on the Arrhenius plot of the reaction rate (r) versus $1/T$, where T represents the temperature.

2.4. Computational details

All density functional theory (DFT) calculations were performed using the Vienna Ab-initio Simulation Package (VASP), and the Bader charge was obtained by the Bader program [26]. Projector augmented wave potential was employed to depict the electron-ion interaction and the exchange-correlation interactions were described by generalized gradient approximation [27,28]. Cut-off energy of 450 eV was set for the expansion of a plane wave basis, and the Brillouin zone was sampled by a Monkhorst-Pack mesh of $3 \times 3 \times 1$ k-point of the supercell. The convergence criterion of the self-consistent field (SCF) is 10^{-5} eV, and the force convergence value of atoms is 0.05 eV/Å. PBE+ U based on the Hubbard U scheme approach was used to describe the strong correlation of the 3d orbitals of Mn cations and 5d orbitals of Ce cations, whose value was set up to 4.0 and 5.0 eV, respectively, according to previous calculation studies [29,30]. The adsorption energies (E_{ads}) are calculated as follows:

$$E_{ads} = E_{(adsorbate+substrate)} - E_{adsorbate} - E_{substrate} \tag{2}$$

The more negative adsorption energy means a stronger interaction, and the density difference ($\Delta\rho$) is defined follow as the formula :

$$\Delta\rho = \rho_{(adsorbate+substrate)} - \rho_{adsorbate} - \rho_{substrate} \tag{3}$$

The work function (Φ) is calculated using Eq. 4 to evaluate the ability

of electrons to escape from a solid surface.

$$\Phi = E_{vacuum} - E_{Fermi} \tag{4}$$

3. Results and discussion

3.1. Physicochemical properties of the catalysts

XRD measurements were implemented to confirm the phase structures of the prepared catalysts, and the results were depicted in Fig. 1a. It can be observed that the X-ray diffraction pattern of Mn$_2$O$_3$ @CeO$_2$ is mainly composed of bixbyite-type α-Mn$_2$O$_3$ (JCPDS #241–1442) and cubic fluorite-type CeO$_2$ (JCPDS #65–2975), and no observed peaks ascribed to the impurity phase is detected, confirming the existence of a two-phase composition of α-Mn$_2$O$_3$ and CeO$_2$. As shown in Fig. 1b, the specific surface area of Mn$_2$O$_3$ @CeO$_2$ (50.7 m^2 g^{-1}) becomes larger than that of pure Mn$_2$O$_3$ (40.7 m^2 g^{-1}). In addition, the BJH pore size distribution results reveal that both Mn$_2$O$_3$ and Mn$_2$O$_3$ @CeO$_2$ display a mesoporous structure with average pore diameters of 18.6 and 5.7 nm, respectively, which can efficiently overcome the molecular diffusion limitation of reactants, intermediates, and products [31].

Subsequently, the morphologies and crystallographic characteristics of obtained samples were further observed by SEM and TEM techniques. SEM images in Fig. S1 show that the bare Mn$_2$O$_3$ display a regular cubic shape structure of around 700 nm (edge length) with a relatively smooth surface. After coating CeO$_2$, the generated Mn$_2$O$_3$ @CeO$_2$ still maintains the cubic morphology (Fig. 1c, d); however, the catalyst surface becomes rough due to the assembly of ultra-small CeO$_2$ nanoparticles. As confirmed by TEM in Fig. 1e, the outer surface of Mn$_2$O$_3$ @CeO$_2$ is successfully wrapped by a thin "layer". Furthermore, the HRTEM pattern depicted in Fig. 1f verifies that the crystalline nature of Mn$_2$O$_3$ @CeO$_2$, in which polycrystalline nanoparticles of bixbyite-type α-Mn$_2$O$_3$ lattice plane ((222); d spacing = 0.262 nm) and fluorite-type CeO$_2$ lattice plane ((111); d spacing = 0.319 nm) can be clearly discerned. These results suggest that more interfaces between Mn$_2$O$_3$ and CeO$_2$ are formed, and the mutual interaction at the manganese–cerium interface can be strongly achieved [32]. Additionally, corresponding EDS mapping results (Fig. 1g–k and S2) clearly reveal that the presence of Mn, Ce, and O elements, wherein Mn is homogeneously distributed in the central region, with the coexistence of Ce on the outer shell. Meanwhile, the CeO$_2$ outer shell is calculated to be 15 nm in thickness. In general, the above studies confirm the successful synthesis of the core-shell geometry of Mn$_2$O$_3$ @CeO$_2$ cubes, which enables good structural and thermocatalytic properties in NO oxidation.

3.2. Catalytic activity and stability

To assess catalytic performance, we exposed prepared catalysts with a commercial reference catalyst (2.0 wt% Pt/γ-Al$_2$O$_3$) to the reactant gas mixture (500 ppm NO, 10 vol% O$_2$, 5 vol% H$_2$O, and 100–300 ppm SO$_2$ when needed and balanced with N$_2$) while raising the reaction temperature from 150° to 400°C to test NO conversion. The activity profiles of NO oxidation over different catalysts are provided in Fig. 2a. The catalytic conversion of NO to NO$_2$ on the prepared catalysts exhibits a volcano profile as a result of the competitive effects between the energy barrier in kinetics and reaction thermodynamic equilibrium [33]. As can be seen, the Mn$_2$O$_3$ @CeO$_2$ catalyst possesses NO conversion performance superior to those of the corresponding pure oxides and the commercial Pt/γ-Al$_2$O$_3$ catalyst throughout the whole operating temperature window. Specially, the highest NO conversion of Mn$_2$O$_3$ @CeO$_2$ catalyst at 275 °C is 85.7 % and has a ~64 % increase over Pt/γ-Al$_2$O$_3$ at 350 °C. The improvement of catalytic behavior is mainly due to the synergistic effect produced by the chemically mixed oxides. Notably, for the conversion of NO to NO$_2$, T_{50} (the half conversion
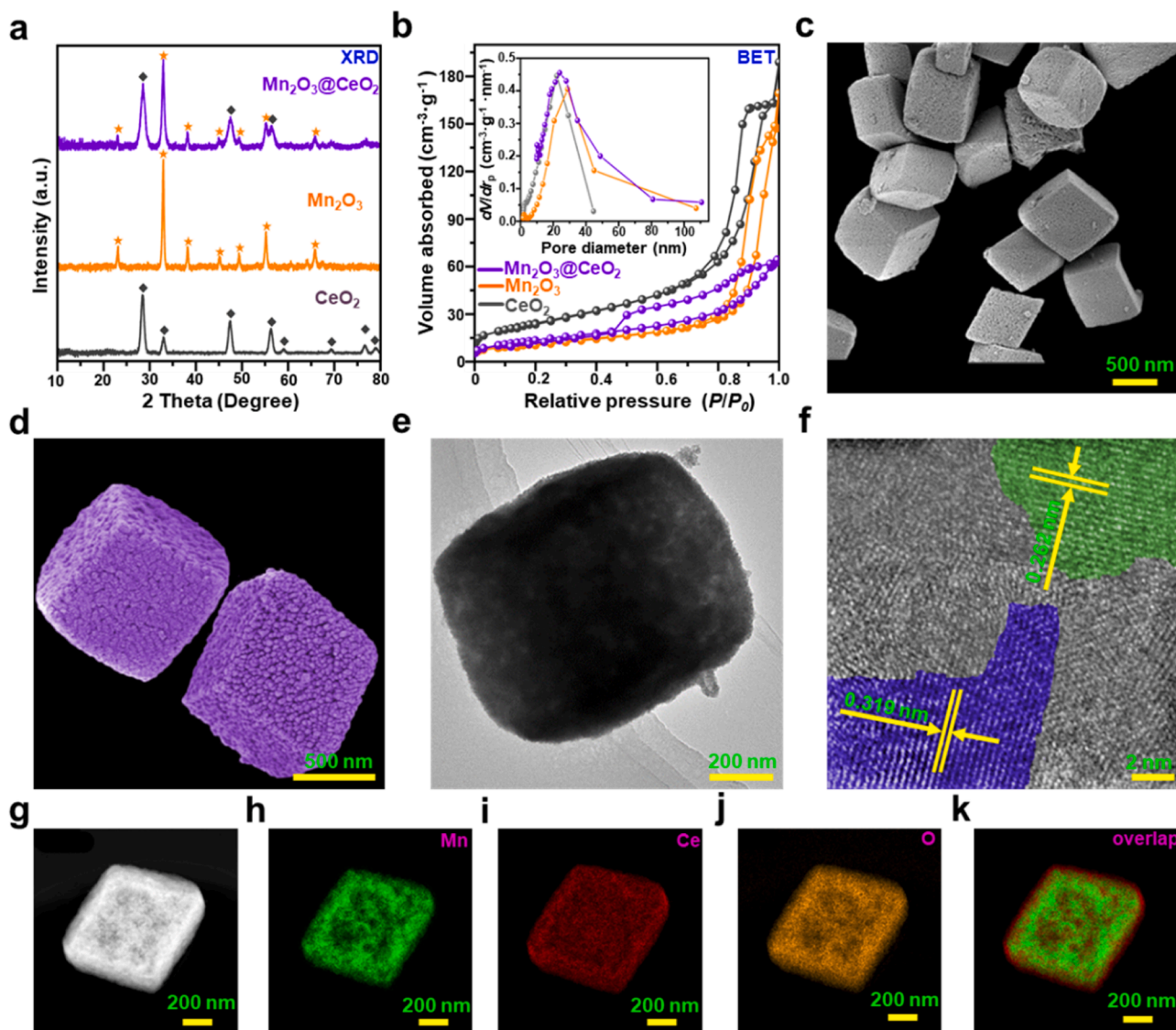
Fig. 1. Structural and morphological analysis of Mn_2O_3 @CeO_2: (a) XRD pattern; (b) N_2 adsorption–desorption isotherms; (c) SEM, (e) TEM, and (f) HRTEM images; (g-k) EDS mapping images.

temperature, Fig. 2b) followed the sequence: Mn_2O_3 @CeO_2 (183 °C) < Mn_2O_3 (256 °C) < CeO_2 (316 °C). Compared with Pt/Al_2O_3, Mn_2O_3 @CeO_2 catalyst reduces the T_{50} as low as 69 °C, and this catalytic performance resembles or even superior to those of many other previously reported materials (Table S2), including Pt/Fe_2O_3 [34], $Pt–Pd/Al_2O_3$ [35], $La_{1-x}Sr_xCoO_3$ [36], and YMn_2O_5 [37]. Kinetic studies of NO oxidation over synthesized samples were further conducted and were presented in Fig. 2c and S3. In compliance with the catalytic activities, Mn_2O_3 @CeO_2 displays the lowest apparent activation energy (E_a = 22.4 kJ mol^{-1}) among the investigated materials, suggesting that NO oxidation reaction over Mn_2O_3 @CeO_2 proceeds more readily than that over the other samples.

In practical working conditions, trace amounts of SO_2 are inevitable components in the coal-fired flue gas, which greatly affects the functionality of the catalysts. Therefore, different contents of SO_2 (100–300 ppm) are introduced to appraise the impact of SO_2 molecules on the activity of Mn_2O_3 @CeO_2 and Mn_2O_3 catalysts. As shown in Fig. 2d, the introduction of SO_2 into the system produced a dramatic drop in the performance of Mn_2O_3 (ca. from 62.0 % to 25.6 %) after 10 h of reaction. Unfortunately, the removal of SO_2 from the system after the experiment did not lead to any significant changes in activity due to the

irreversible SO_2 poisoning of Mn_2O_3. In comparison, the addition of SO_2, even increasing to a high concentration (300 ppm), shows negligible impacts on the activity of Mn_2O_3 @CeO_2. These results demonstrate that the Mn_2O_3 @CeO_2 catalyst exhibits excellent SO_2 tolerance. Moreover, the H_2O-resistant performance of the prepared catalysts was also investigated. When 5 vol% water vapor is introduced into the feed gas, drops in NO conversion of ca. 4.8 % and 12.3 % are detected over Mn_2O_3 @CeO_2 and Mn_2O_3 catalysts, respectively (Fig. S4). When water vapor is removed from the reactor, the NO conversion is immediately recovered to the original value. In addition, the cycling stability test of Mn_2O_3 @CeO_2 was carried out under the same reaction conditions at 275 °C. As shown in Fig. S5, no significant change in the activities of Mn_2O_3 @CeO_2 is observed in the three cycling tests, confirming a satisfactory stability. Meanwhile, the crystal structure and morphological feature of the used sample keep intact after the cycling stability test (Figs. S6 and S7), manifesting the structural stability of the Mn_2O_3 @CeO_2 catalyst. Based on the above test and data, it can be inferred that CeO_2 coating modification can effectively improve the low-temperature activity and SO_2 tolerance of Mn_2O_3 @CeO_2 catalyst for NO oxidation.
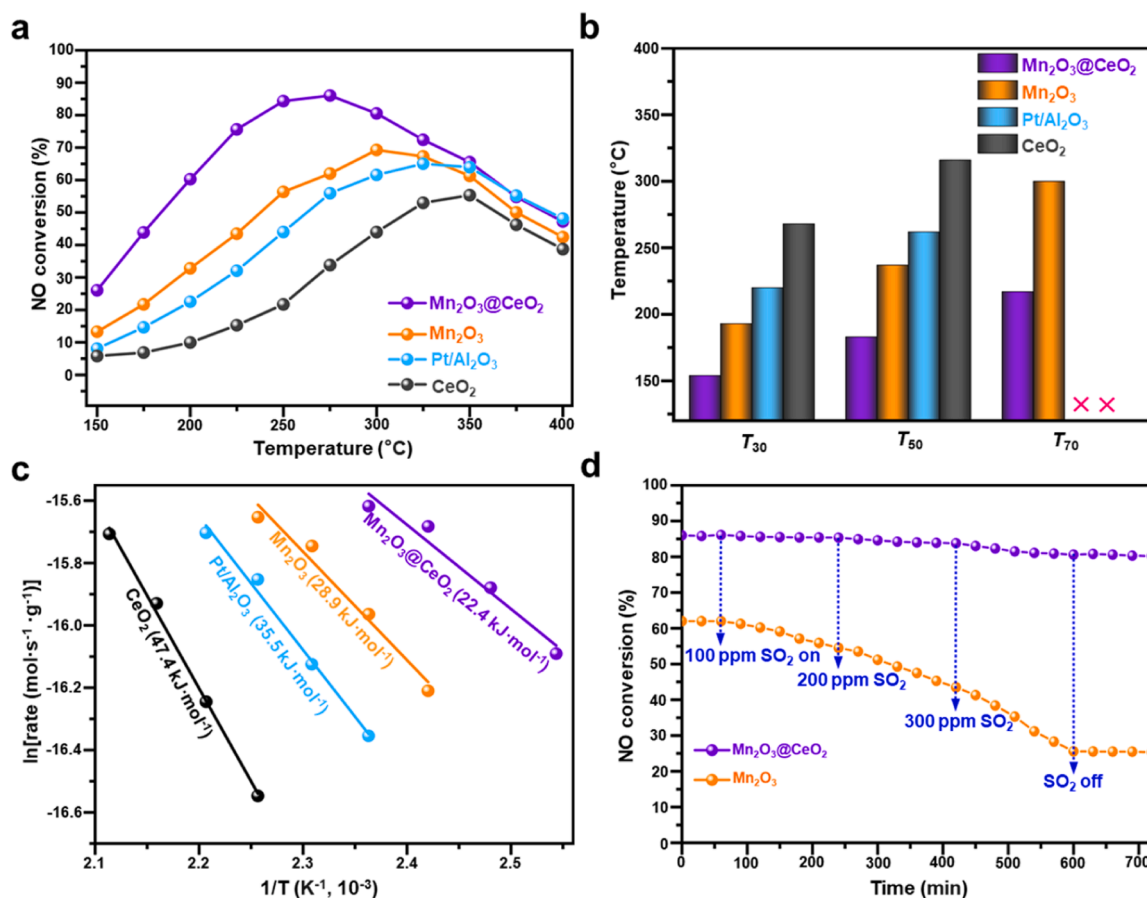
Fig. 2. (a, b) NO conversion versus the reaction temperature of prepared samples; (c) Arrhenius plots; (d) SO$_2$ tolerance test of Mn$_2$O$_3$ @CeO$_2$ and Mn$_2$O$_3$ catalysts. Reaction conditions: NO= 500 ppm, O$_2$ = 10 vol%, balanced with N$_2$, total flow rate of 300 mL min^{-1}, GHSV= 90,000 h^{-1}.

3.3. Formation of Mn^{4+}-O-Ce^{3+} interfacial sites

The surface element composition and valence distribution of prepared samples were investigated by the XPS technique, with their spectra and quantitative values shown in Fig. 3a–c. As depicted in Fig. 3a, the Ce 3d spectrum displays ten well-resolved peaks that are assigned to Ce 3$d_{5/2}$ (labeled as V-kind) and Ce 3$d_{3/2}$ states (labeled as U-kind). The peaks labeled V', V^0, U' and U^0 correspond to Ce^{3+}, while the rest peaks can be classified as Ce^{4+} [38,39]. The high-resolution Mn 2$p_{3/2}$ spectrum in Fig. 3b can be fitted into three individual subbands of Mn^{2+} (641.1 eV), Mn^{3+} (642.4 eV), and Mn^{4+} (644.5 eV), respectively. According to the fitting results, the Mn$_2$O$_3$ @CeO$_2$ exhibits a higher ratio of Ce^{3+} (22.7 %) in comparison with pure CeO$_2$ (16.5 %), suggesting that more unsaturated chemical bonds are produced in the CeO$_2$ coating process. Meanwhile, the Mn^{4+}/Mn$_{total}$ ratio of Mn$_2$O$_3$ @CeO$_2$ catalyst (34.3 %) is significantly higher than that of pure Mn$_2$O$_3$ (28.7 %), and it is well demonstrated that Mn^{4+} species own a higher redox ability than other Mn species and contributes greatly to the oxidation reaction [40]. Hence, the valence state of the Mn species is increased, while it is decreased for Ce species compared with the Mn$_2$O$_3$ @CeO$_2$ and CeO$_2$ catalysts, respectively. These phenomena can infer that a valency-degeneracy exists in the interfacial perimeter of Mn$_2$O$_3$ @CeO$_2$ catalyst via Ce^{4+} + Mn^{3+} ↔ Ce^{3+} + Mn^{4+}. To validate the above experimental findings and gain a deeper understanding of the interaction between Mn$_2$O$_3$ and CeO$_2$, charge density difference and work function calculations were carried out and the results are presented in Fig. S8. Notably, the charge density difference results reveal a noticeable charge transfer from the Mn$_2$O$_3$ cluster to the CeO$_2$ substrate, which indicates that the two materials mutually interact. Additionally, the work function results further provide even more support for the

conclusion that there exists a mutual interaction between the two materials. Specifically, the electrons tend to flow from the low work function (ΦMn$_2$O$_3$ = 4.85 eV) to the high work function (ΦCeO$_2$ = 5.60 eV) to make a charge balance at the CeO2/Mn2O3 interfaces., as the electrons tend to flow from low work function to the high work function to make a charge balance at the CeO$_2$/Mn$_2$O$_3$ interfaces [41]. O 1 s spectrum in Fig. 3c suggests the existence of multiple oxygen species in prepared catalysts. Commonly, the O 1 s region can be deconvoluted into three components at 532.6, 530.7, and 528.8 eV, respectively ascribed to the adsorbed hydroxyl groups or water (O$_\gamma$), oxygen species adsorbed in oxygen vacancies (O$_\beta$), and lattice oxygen (O$_\alpha$). The quantitative results show that the Mn$_2$O$_3$ @CeO$_2$ own the highest O$_\beta$ fraction (31.2 %), followed by the Mn$_2$O$_3$ (26.5 %) and CeO$_2$ (19.6 %). As reported by previous literature [42], the O$_\beta$ species is tightly related to the defect sites with low oxygen coordination. On the basis of the above XPS and DFT analysis, it can conclude that a high percentage of oxygen vacancies are formed to maintain electrostatic balance due to the electrons transfer from the Mn to Ce at the manganese–ceria interfaces.

Raman spectroscopy was collected to study the structural features of prepared catalysts. As depicted in Fig. S9, several obvious characteristic bands centered for pure CeO$_2$ at 462 cm^{-1} correspond to the symmetrical stretching mode of the Ce–O vibrational unit, while the bands at 338 and 636 cm^{-1} detected for the Mn$_2$O$_3$ sample can be assigned to the bending vibration and symmetric stretching vibration of Mn–O–Mn bond in [MnO$_6$] octahedral, respectively [43,44]. In comparison with the two counterparts, three peaks of Mn$_2$O$_3$ @CeO$_2$ hybrid shift to the low wavenumbers, suggesting that both Mn–O and Ce–O are weakened by the generated Mn–O–Ce structure [45]. This new structure can give rise to a change in the electronic structure and promote the formation of reactive oxygen species on the catalyst surface [46]. Meanwhile, the
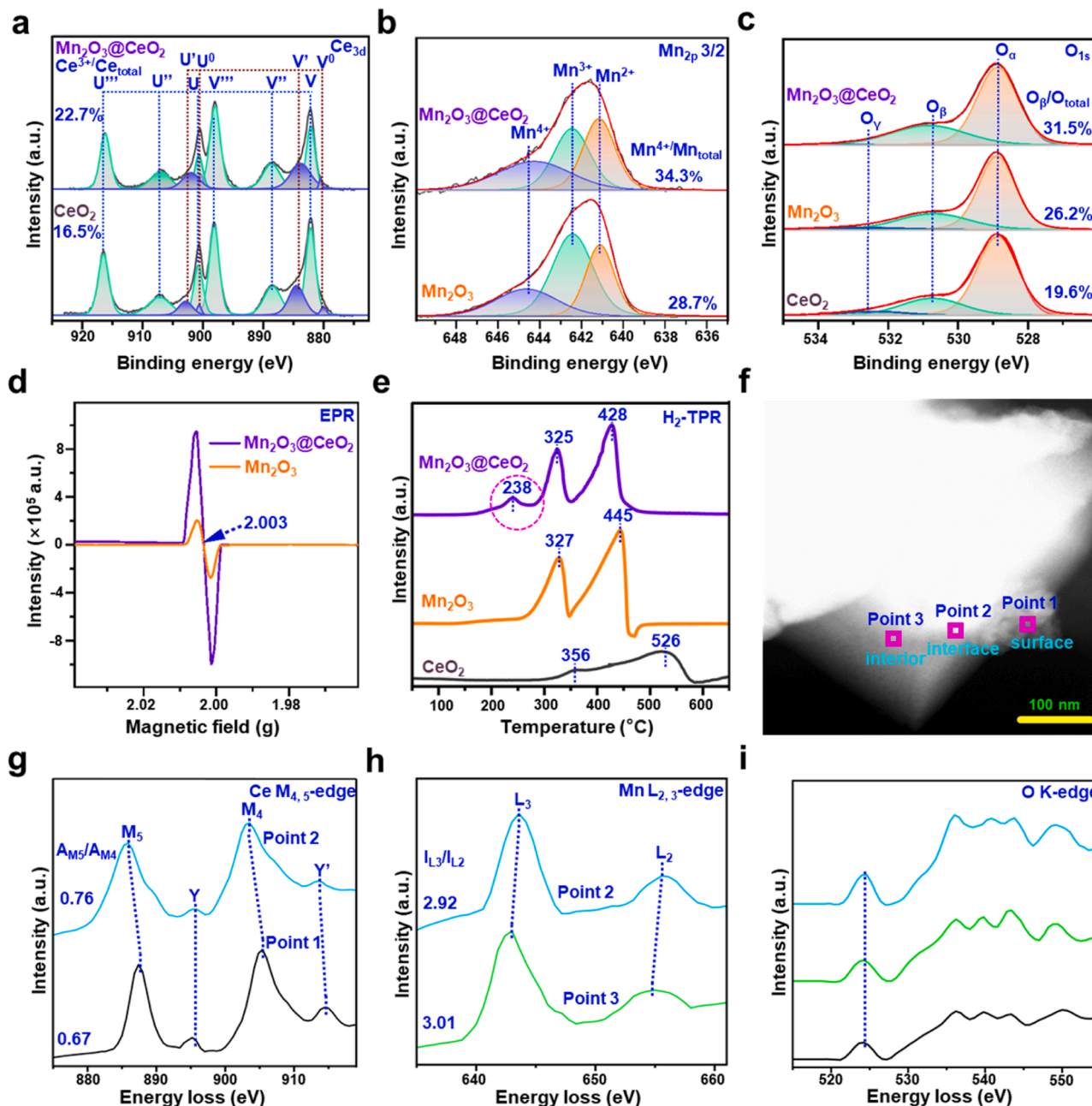
Fig. 3. XPS spectra of prepared samples: (a) Ce 3*d*, (b) Mn 2*p* 3/2, and (c) O 1*s* orbitals; (d) Low-temperature EPR spectrum; (e) H_2-TPR of prepared samples; (f) SAC-STEM HAADF images and point scanning EELS spectrum of (g) Ce $M_{4, 5}$-edge, (h) Mn $L_{2, 3}$-edge, and (i) O K-edge over Mn_2O_3 @CeO_2 sample.

Mn–O bond strength is assessed by bond force constant (*k*) according to Hooke's law [47]:

$$w = \frac{1}{2\pi c} \sqrt{\frac{k}{\mu}} \qquad (5)$$

Wherein ω, *c*, and μ stands for the Raman shift of Mn-O stretching vibration, light velocity, and effective mass, respectively. As observed in the inset of Fig. S9, the bond force constant of Mn_2O_3 @CeO_2 (290.2 N·m^{-1}) is slightly lower than that of pure Mn_2O_3 (293.0 N·m^{-1}), indicating that the lattice oxygen reactivity is enhanced after CeO_2 coating. To validate the presence of oxygen vacancies, low-temperature EPR measurements were conducted and the results were plotted in Fig. 3d. EPR spectra show that the prepared samples exhibit a typical signal with *g* values of 2.003, which is attributed to the unpaired electrons trapped in the oxygen vacancy. Apparently, the signal intensity of

Mn_2O_3 @CeO_2 hybrid is higher than that of pure Mn_2O_3, disclosing that the CeO_2 sheath can significantly facilitate the generation of oxygen vacancies.

To gain more nuanced insight into the reducibility of the prepared samples, H_2-TPR technique was carried out and the results are presented in Fig. 3e. It can be evidently observed that CeO_2 also displays two hydrogen consumption peaks located at 356 and 526 °C, which are assigned to the surface oxygen of stoichiometric cerium (Ce^{4+}–O–Ce^{4+}) and nonstoichiometric cerium (Ce^{3+}–O–Ce^{4+}). By contrast, Mn_2O_3 exhibited two hydrogen consumption peaks centered at 327 and 445 °C, originating from the reduction of $Mn_2O_3 \rightarrow Mn_3O_4$ and $Mn_3O_4 \rightarrow MnO$, respectively. Two reductive peaks of Mn_2O_3 shift toward lower temperature for Mn_2O_3 @CeO_2, implying the improvement of the oxidizability of Mn_2O_3 in Mn_2O_3 @CeO_2. More encouragingly, a new hydrogen consumption peak at low temperature (238 °C) is observed for the

Mn_2O_3 @CeO_2 catalyst, and this implies that the synergetic effect between Mn_2O_3 and CeO_2 components can give rise to an enhancement of the low-temperature redox properties of the prepared sample. More precisely, the intimate contact between Mn_2O_3 and CeO_2 linked by the "Ce-O-Mn" bonds can result in an electron-acceptor like state and accelerate the electronic transport abilities in the thermo-catalysis reaction [48]. The O_2-TPD curves in Fig. S10 point out that, in the temperature region of 50–250 °C, the intensity of desorbed oxygen species for the obtained samples decreases in the order: Mn_2O_3 @CeO_2 > Mn_2O_3 > CeO_2, implying that the strong interactions between Mn_2O_3 and CeO_2 can enrich the density of O_{ads} and boost the mobility of O_{latt}, thus facilitating the low-temperature adsorption and activation of O_2 molecules on the surface of catalysts during the catalytic reaction.

SAC-STEM HAADF images combined with point scanning EELS spectrum were employed to reveal the viability of chemical states and collective interaction at the interface in the vicinity of CeO_2–Mn_2O_3 nanocubes [49]. In HAADF images (Fig. 3f), a sharp interface between Mn_2O_3 core and CeO_2 shell is clearly observed. Points 1–3 are selected to investigate the change of physicochemical characteristics of surface to bulk, wherein points 1, 2, and 3 represent the surface, interface, and

bulk, respectively. As illustrated in Fig. 3g, the Ce-$M_{4,5}$ edges arise from transitions between $3d^{10}4f^n$ to $3d^94f^{n+1}$ states coupled with the valence-sensitive fine spectrum, and the satellite peaks Y and Y' are ascribed to the delocalization of the f-electrons. By comparing the reference Ce-$M_{4,5}$ spectra from CeO_2 and Ce_2O_3 [50], the valence states of Ce species in the surface (points 1) and interface (points 2) are roughly estimated to be 4.00 and 3.67, confirming that a portion of Ce species is reduced at CeO_2/Mn_2O_3 interface. Judging from the measurement of Mn-$L_{2,3}$ edges (Fig. 3h), the valence states of Mn species at CeO_2/Mn_2O_3 interface (3.12) is much higher than that at the Mn_2O_3 core (3.00), further verifying the above-mentioned conclusion that a valency-degeneracy exists at Mn_2O_3 @CeO_2 interfacial perimeter. It is well accepted that the pre-edge of the O K-edge spectra can reflect the electrons transfer from the O 1 s orbital to the unoccupied 2p orbital hybridized with transitional metal (TM) ions [51]. As shown in Fig. 3i, the reduced pre-edge and split shoulder peak at higher energy signifies that a large number of uncoordinated TM–O are generated at the CeO_2/Mn_2O_3 interfaces, indicating the presence of oxygen vacancies that corresponded to the above EPR analysis.

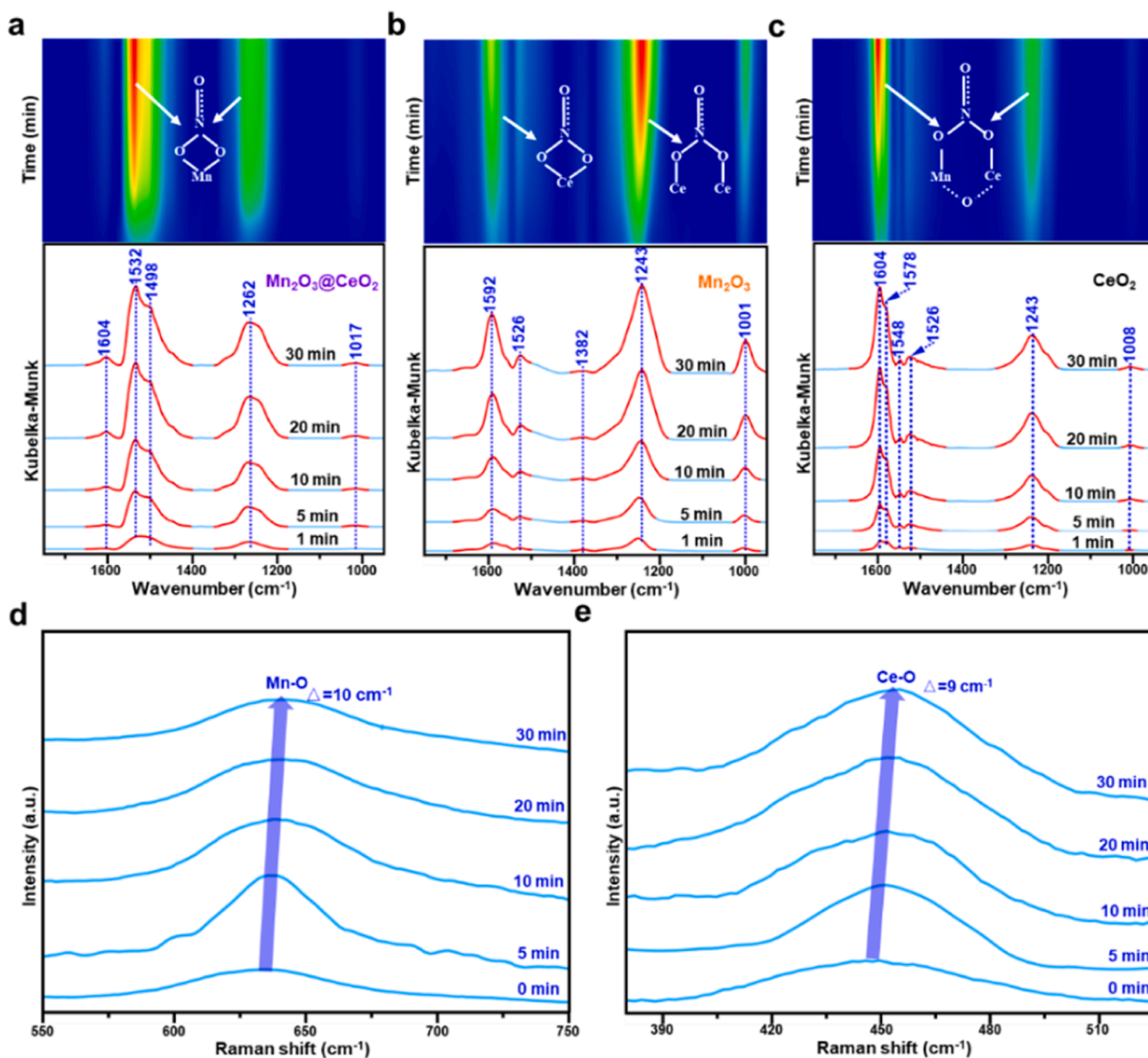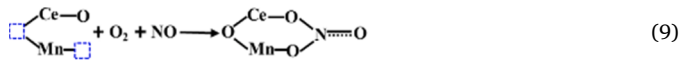For transition metal oxides, it is widely recognized that oxygen

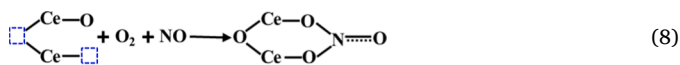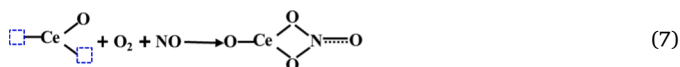**Fig. 4.** *In situ* DRIFT spectra and the corresponding mapping results of (a) Mn_2O_3, (b) CeO_2, and (c) Mn_2O_3 @CeO_2 exposed to NO + O_2 at 275 °C; *In situ* Raman spectra of NO oxidation over Mn_2O_3 @CeO_2 at 275 °C: (d) Mn–O and (e) Ce–O.

defects play a significant role in the NO-to-NO$_2$ oxidation capacity. In order to further investigate this relationship, we propose a more extensive analysis of the structure-activity relationship of prepared samples for NO oxidation activities. In support of this, Fig. S11 demonstrates a clear correlation between the reaction rate and O$_\beta$/O$_{total}$ ratio. Previous studies have suggested that the high mobility of oxygen species is a key factor in the adsorption and activation of gas-phase oxygen [52]. Hence, it is possible to achieve continuous conversion of oxygen species at a low-temperature range.

3.4. Identification of reactive intermediates and active sites

To further expound the N-containing species formed on the catalyst surface, in situ DRIFTS measurements were implemented. After introducing a dilute stream of the 500 ppm NO + 10 vol% O$_2$ to the reaction cell, abundant bidentate Mn-nitrate (1532/1262 cm^{-1}; Eq. 6) and monodentate Mn-nitrate (1498 cm^{-1}) along with the bridged Mn-nitrate (1604/1017 cm^{-1}) are detected on Mn$_2$O$_3$ surface (Fig. 4a), and the intensity of stretching bands at 1532/1262 and 1498 cm^{-1} increases with the prolonging of reaction time [30,53]. Fig. 4b shows the DRIFT spectra of NO$_x$ adsorption over CeO$_2$, which is much different from that of Mn$_2$O$_3$. Several distinct bands appear at 1592, 1526/1001, 1382, and 1243 cm^{-1}, which are respectively assigned to the bidentate Ce-nitrate (Eq. 7), monodentate Ce-nitrate, ionic Ce-nitrate, and bridging Ce-nitrate (Eq. 8) [14,54]. Nevertheless, a quite different observation is found for the Mn$_2$O$_3$ @CeO$_2$ catalyst (Fig. 4c). Besides the above-observed bands (1604/1008, 1526, and 1243 cm^{-1}), two newly formed bands at 1578 and 1548 cm^{-1} are detected, which belong to the characteristic bands of chelating bidentate Mn-nitrate [55]. Notably, it is worth emphasizing that the N-containing species over Mn$_2$O$_3$ @CeO$_2$ are mainly in the form of bridging nitrate, manifesting that the formation of intermediates is inclined formed on the Mn$_2$O$_3$-CeO$_2$ heterojunction interface according to the Eq. 9.

$$\square{-}Mn\!\!\begin{array}{c}O\\O\end{array} + O_2 + NO \longrightarrow O{-}Mn\begin{array}{c}O\\\\N\!\!=\!\!=\!\!=O\end{array} \qquad (6)$$

$$\square{-}Ce\!\!\begin{array}{c}O\\O\end{array} + O_2 + NO \longrightarrow O{-}Ce\begin{array}{c}O\\\\N\!\!=\!\!=\!\!=O\\O\end{array} \qquad (7)$$

$$\begin{array}{c}Ce{-}O\\Ce{-}\square\end{array} + O_2 + NO \longrightarrow O\begin{array}{c}Ce{-}O\\\\N\!\!=\!\!=\!\!=O\\Ce{-}O\end{array} \qquad (8)$$

$$\begin{array}{c}Ce{-}O\\Mn{-}\square\end{array} + O_2 + NO \longrightarrow O\begin{array}{c}Ce{-}O\\\\N\!\!=\!\!=\!\!=O\\Mn{-}O\end{array} \qquad (9)$$
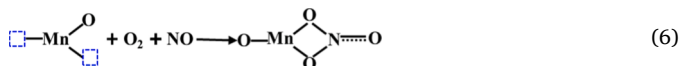
In order to monitor the dynamic variation of the Mn$_2$O$_3$ @CeO$_2$ interfaces under real reaction conditions, in situ Raman spectroscopy was implemented and the detailed results are presented in Fig. 4d and e. The sample is firstly pretreated under argon at 275 °C for 30 min. Then, the intensities of Mn–O and Ce–O Raman band increase instantly upon the NO + O$_2$ switch, and further decline as the time prolongs. Meanwhile, a synchronous shift is observed for the signals corresponding to Mn-O ($\Delta = 10$ cm^{-1}) and Ce-O ($\Delta = 9$ cm^{-1}) sites with the increase of the reaction time. Such results verify both Mn-O and Ce-O bonds contribute greatly to the conversion of NO molecules. From the viewpoint of structural evolution and reactive intermediates, it can be concluded that the strong interaction at the manganese–cerium interfaces, in a chemical environment of "Mn–O$_v$–Ce", shows a positive impact on the activation of reactant molecules during the NO oxidation reaction, thus resulting in an improvement of low-temperature activity.

3.5. Insight into the inhibition effect of SO$_2$ deactivation

To elucidate inherent reasons why the Mn$_2$O$_3$ @CeO$_2$ catalyst displays a superior SO$_2$ tolerance, in situ DRIFTS of SO$_2$ adsorption experiments were performed to detect the existence states of sulfate species deposited on prepared catalysts, and the results are shown in Fig. 5. After introducing SO$_2$ to the pure Mn$_2$O$_3$ catalyst for 1 min, the characteristic peak of the monodentate sulfate (1600/1039 cm^{-1}), co-ordinated sulfate (1285 cm^{-1}), bisulfate (1215 cm^{-1}), and hydrated SO$_2$ (1136 cm^{-1}) are observed. With the prolonging of reaction time, the peak intensity of coordinated sulfate, bisulfate, and hydrated SO$_2$ gradually increases and becomes dominant. When the pure CeO$_2$ is exposed to the SO$_2$, the characteristic bands of surface sulfate species (asymmetric stretching of S = O: 1345/1289 cm^{-1}; symmetric stretching of S-O: 1115/998/924/907 cm^{-1}) are observed [56,57]. Moreover, a trace of bulk sulfates located at 1205 cm^{-1} is detected after about 10 min. Interestingly, in the case of Mn$_2$O$_3$ @CeO$_2$ catalyst, after introducing SO$_2$ for 30 min, abundant Ce-related sulfates (symmetric stretching of S-O and bulk sulfates) with negligible Mn-related sulfates are detected, indicating that SO$_2$ prefers to bond with Ce element rather than Mn element to generate sulfate species, which inhibits the poisoning of active sites in the core of Mn$_2$O$_3$ @CeO$_2$ catalyst.

To probe into the anti-SO$_2$-poisoning mechanism for the Mn$_2$O$_3$ @CeO$_2$ catalyst, theoretical calculations based on density functional theory (DFT) were conducted. As shown in Fig. 5d and S12, there exist three stable adsorption configurations on CeO$_2$ (111) surface. The adsorption energies for SO$_2$ on CeO$_2$ (111) surface are in the range of –1.87 – –3.48 eV, and obvious Ce-O bonds can be observed between the surface Ce atoms and the O atoms of SO$_2$ molecule, indicating strong chemisorption on the CeO$_2$ surface. The average S-O bond lengths are enlarged from 1.45 Å (SO$_2$ molecule in the gas phase) to 1.52, 1.72, and 1.61 Å, respectively. Meanwhile, four stable SO$_2$ adsorption configurations are obtained after considering all possible adsorption sites, the interaction between SO$_2$ and the Mn$_2$O$_3$ surface are less intense than that on CeO$_2$ surface since the adsorption energies are all less than 1 eV (Fig. 5e and S13). It can be seen that S-O bonds for SO$_2$ are almost the same, the average lengths for S-O bonds on Mn$_2$O$_3$ surface are 1.51, 1.45, 1.45, and 1.45 Å, respectively. According to the above-mentioned analysis, it can be seen that the adsorption energies of SO$_2$ on CeO$_2$ surface are much larger than those on the Mn$_2$O$_3$ surface, indicating that SO$_2$ molecule is more inclined to bond with the CeO$_2$ species of the catalyst. Fig. 5f gives the charge density difference maps for the SO$_2$ adsorption configurations, as well as the Bader charge of SO$_2$ before and after adsorption. It clearly indicates that the charge transfer between SO$_2$ molecule and the CeO$_2$ surface is much stronger than that on the Mn$_2$O$_3$ surface, which is also confirmed by the Bader charge analysis. On CeO$_2$ surface, 0.49 e of charge of S atom is transferred to the surface, while on Mn$_2$O$_3$ surface the S atom of SO$_2$ gains 1.73 e. Moreover, the change of Bader charge for the O atoms of SO$_2$ molecule on Mn$_2$O$_3$ surface is more subtle than that on the CeO$_2$ surface, indicating that the charge transfer between SO$_2$ and CeO$_2$ species is stronger than that between SO$_2$ and Mn$_2$O$_3$. Therefore, summarizing the adsorption manners and charge transfer situation of SO$_2$ on CeO$_2$ and Mn$_2$O$_3$ surfaces using DFT, it can be inferred that SO$_2$ molecule has a stronger affinity to the CeO$_2$ shell than that to the Mn$_2$O$_3$ core.

In addition, the Mn$_2$O$_3$ @CeO$_2$ after 15 h of exposure to a sulfur contaminated flue gas was further examined by the TEM and EDS mapping techniques. Fig. 5g shows that no apparent morphological changes are observed in the sulfated Mn$_2$O$_3$ @CeO$_2$ sample Meanwhile, the EDS results (Fig. 5h–k) display that the S element mainly accumulates on the CeO$_2$ shell, while it is relatively sparse on the internal cavity of Mn$_2$O$_3$. These phenomena suggested that the CeO$_2$ shell serves as a sacrifice that can effectively inhibit the blocking of active sites in the seeded core, which is consistent with in situ drifts analysis and DFT calculations.

4. Conclusions

In summary, we have successfully synthesized a bifunctional Mn$_2$O$_3$ @CeO$_2$ core–shell catalyst for the thermochemical conversion of NO to
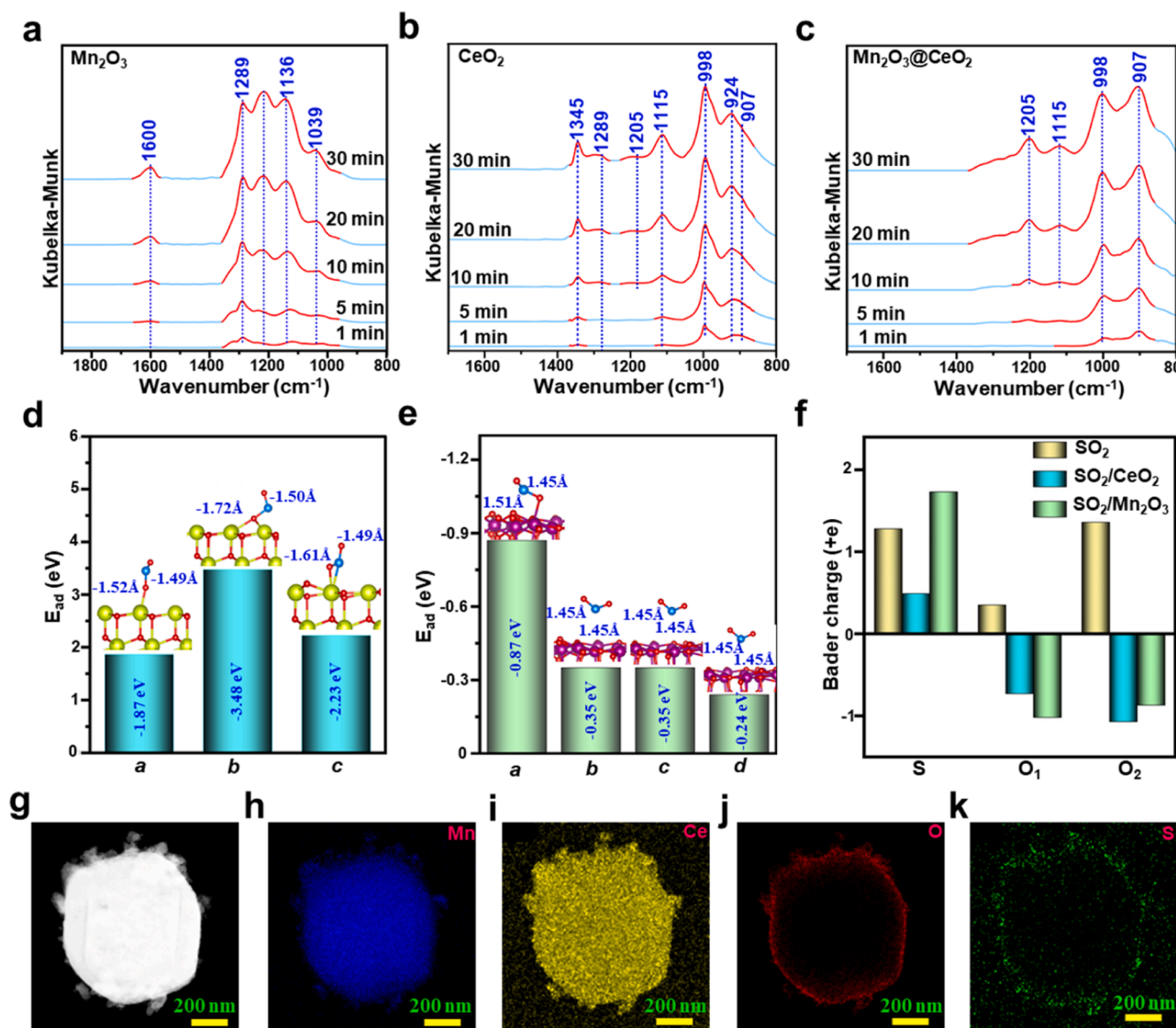
Fig. 5. *In-situ* spectra results of (a) Mn_2O_3, (a) CeO_2 and (b) Mn_2O_3 @CeO_2 exposed to SO_2 at 275 °C; (d, e) adsorption energies of O_2 over CeO_2 and Mn_2O_3 models; (f) Bader charge of SO_2, CeO_2 and SO_2, Mn_2O_3; (g-k) EDS mapping images of sulfated Mn_2O_3 @CeO_2.

NO_2. The obtained Mn_2O_3 @CeO_2 composite exhibits excellent low-temperature catalytic activity (T_{50} at 183 °C and T_{86} at 275 °C), significantly lower than that of commercial Pt/Al_2O_3 catalyst (T_{50} at 262 °C). Comprehensive experimental results suggest that Mn_2O_3 @CeO_2 composite establishes the interfacial electron transfer channels through the "Mn-O_v-Ce" bond to adsorb/activate the reactive intermediates and resulting in improved catalytic activity. Meanwhile, a higher affinity of SO_2 to the CeO_2 sheath than that to the Mn_2O_3 core, can effectively restrain the generation of Mn-related sulfate species that block the active sites, endowing the Mn_2O_3 @CeO_2 a superior SO_2 resistance. This work opens a novel perspective for guiding the development of highly-efficient NO oxidation catalysts for air-pollutant remediation and beyond. Moving forward, further investigations on the prepared Mn_2O_3 @CeO_2 material are necessary to improve its water resistance towards practical industrial applications.

CRediT authorship contribution statement

Lei Chen: Formal analysis, Writing – original draft, Writing – review & editing, Visualization. **Dan Ren, Xiaoke Hou, Jinping Zhang, Yangwen Wu, Yibo Wang, and Chao Hu:** Methodology, Investigation. **Chao Li & Ching-Yu Chiang:** Methodology. **Peigao Duan, Chi He,** **Qiang Lu:** Supervision, Writing – review & editing, Project administration, Funding acquisition.

Declaration of Competing Interest

The authors declare that they have no known competing financial interests or personal relationships that could have appeared to influence the work reported in this paper.

Data availability

Data will be made available on request.

Appendix A. Supporting information

Supplementary data associated with this article can be found in the online version at doi:10.1016/j.apcatb.2023.123202.

References

[1] S. Schönebaum, J. Dornseiffer, P. Mauermann, B. Wolkenar, S. Sterlepper, E. Wessel, R. Iskandar, J. Mayer, T.E. Weirich, S. Pischinger, O. Guillon, U. Simon, Composition/performance evaluation of lean NOₓ trap catalysts for coupling with SCR technology, ChemCatChem 13 (2021) 1787–1805.

[2] Z. Chen, M. Wang, J. Wang, C. Wang, J. Wang, W. Li, M. Shen, Investigation of crystal size effect on the NOₓ storage performance of Pd/SSZ-13 passive NOₓ adsorbers, Appl. Catal. B 291 (2021), 120026.

[3] X. Fang, Y. Liu, Y. Cheng, W. Cen, Mechanism of Ce-modified birnessite-MnO₂ in promoting SO₂ poisoning resistance for low-temperature NH₃-SCR, ACS Catal. 11 (2021) 4125–4135.

[4] D. He, X. Ding, S. Li, Y. Liang, Y. Liu, M. Zhao, J. Wang, Y. Chen, Constructing a Pt/ YMn₂O₅ interface to form multiple active centers to improve the hydrothermal stability of NO oxidation, ACS Appl. Mater. Interfaces 14 (2022) 20875–20887.

[5] A. Buzková Arvajová, P. Boutikos, R. Pečinka, P. Kočí, Global kinetic model of NO oxidation on Pd/γ-Al₂O₃ catalyst including PdOₓ formation and reduction by CO and C₃H₆, Appl. Catal. B 260 (2020), 118141.

[6] S. Adjimi, J.M. García-Vargas, J.A. Díaz, L. Retailleau, S. Gil, M. Pera-Titus, Y. Guo, A. Giroir-Fendler, Highly efficient and stable Ru/K-OMS-2 catalyst for NO oxidation, Appl. Catal. B 219 (2017) 459–466.

[7] P. Zhang, H. Lu, Y. Zhou, L. Zhang, Z. Wu, S. Yang, H. Shi, Q. Zhu, Y. Chen, S. Dai, Mesoporous MnCeOₓ solid solutions for low temperature and selective oxidation of hydrocarbons, Nat. Commun. 6 (2015) 8446.

[8] X.-M. Zhang, Y.-Q. Deng, P. Tian, H.-H. Shang, J. Xu, Y.-F. Han, Dynamic active sites over binary oxide catalysts: In situ/operando spectroscopic study of low-temperature CO oxidation over MnOₓ-CeO₂ catalysts, Appl. Catal. B 191 (2016) 179–191.

[9] Z. Song, S. Yu, H. Liu, Y. Wang, C. Gao, Z. Wang, Y. Qin, Y. Peng, J. Li, Carbon/ chlorinate deposition on MnOₓ-CeO₂ catalyst in chlorobenzene combustion: the effect of SCR flue gas, Chem. Eng. J. 433 (2022), 133552.

[10] J. Shi, H. Li, A. Genest, W. Zhao, P. Qi, T. Wang, G. Rupprechter, High-performance water gas shift induced by asymmetric oxygen vacancies: gold clusters supported by ceria-praseodymia mixed oxides, Appl. Catal. B 301 (2022), 120789.

[11] B. Murugan, A.V. Ramaswamy, D. Srinivas, C.S. Gopinath, V. Ramaswamy, Nature of manganese species in Ce₁₋ₓMnₓO₂₋δ solid solutions synthesized by the solution combustion route, Chem. Mater. 17 (2005) 3983–3993.

[12] T. Rao, M. Shen, L. Jia, J. Hao, J. Wang, Oxidation of ethanol over Mn–Ce–O and Mn–Ce–Zr–O complex compounds synthesized by sol–gel method, Catal. Commun. 8 (2007) 1743–1747.

[13] W. Yang, Y. Liu, Q. Wang, J. Pan, Removal of elemental mercury from flue gas using wheat straw chars modified by Mn-Ce mixed oxides with ultrasonic-assisted impregnation, Chem. Eng. J. 326 (2017) 169–181.

[14] G. Qi, R.T. Yang, R. Chang, MnOₓ-CeO₂ mixed oxides prepared by co-precipitation for selective catalytic reduction of NO with NH₃ at low temperatures, Appl. Catal. B 51 (2004) 93–106.

[15] M. Wang, X. Hong, J. Chen, J. Li, X. Chen, J. Mi, Z. Liu, S. Xiong, Two-step hydrothermal synthesis of highly active MnOₓ-CeO₂ for complete oxidation of formaldehyde, Chem. Eng. J. 440 (2022), 135854.

[16] D. Delimaris, T. Ioannides, VOC oxidation over MnOₓ–CeO₂ catalysts prepared by a combustion method, Appl. Catal. B 84 (2008) 303–312.

[17] K. Yu, L.-L. Lou, S. Liu, W. Zhou, Asymmetric oxygen vacancies: the intrinsic redox active sites in metal oxide catalysts, Adv. Sci. 7 (2020) 1901970.

[18] A. Chen, X. Yu, Y. Zhou, S. Miao, Y. Li, S. Kuld, J. Sehested, J. Liu, T. Aoki, S. Hong, M.F. Camellone, S. Fabris, J. Ning, C. Jin, C. Yang, A. Nefedov, C. Wöll, Y. Wang, W. Shen, Structure of the catalytically active copper–ceria interfacial perimeter, Nat. Catal. 2 (2019) 334–341.

[19] S. Zhao, D. Kang, Y. Liu, Y. Wen, X. Xie, H. Yi, X. Tang, Spontaneous formation of asymmetric oxygen vacancies in transition-metal-doped CeO₂ nanorods with improved activity for carbonyl sulfide hydrolysis, ACS Catal. 10 (2020) 11739–11750.

[20] D. Lee, X. Gao, L. Sun, Y. Jee, J. Poplawsky, T.O. Farmer, L. Fan, E.-J. Guo, Q. Lu, W.T. Heller, Y. Choi, D. Haskel, M.R. Fitzsimmons, M.F. Chisholm, K. Huang, B. Yildiz, H.N. Lee, Colossal oxygen vacancy formation at a fluorite-bixbyite interface, Nat. Commun. 11 (2020) 1371.

[21] Y. Gao, H. Yang, Y. Bai, C. Wu, Mn-based oxides for aqueous rechargeable metal ion batteries, J. Mater. Chem. 9 (2021) 11472–11500.

[22] H. Yan, S. Yao, J. Wang, S. Zhao, Y. Sun, M. Liu, X. Zhou, G. Zhang, X. Jin, X. Feng, Y. Liu, X. Chen, D. Chen, C. Yang, Engineering Pt-Mn₂O₃ interface to boost selective oxidation of ethylene glycol to glycolic acid, Appl. Catal. B 284 (2021), 119803.

[23] J. Huang, H. Zhang, Mn-based catalysts for sulfate radical-based advanced oxidation processes: a review, Environ. Int. 133 (2019), 105141.

[24] R. Cai, Y. Du, S. Peng, H. Bi, W. Zhang, D. Yang, J. Chen, T.M. Lim, H. Zhang, Y. C. Cao, Q. Yan, Synthesis of porous, hollow metal MCO₃ (M=Mn, Co, Ca) microstructures and adsorption properties thereof, Eur. J. Chem. 20 (2014) 421–425.

[25] S. Li, B. Huang, C. Yu, A CeO₂-MnOₓ core-shell catalyst for low-temperature NH₃-SCR of NO, Catal. Commun. 98 (2017) 47–51.

[26] G. Kresse, J. Furthmüller, Efficiency of ab-initio total energy calculations for metals and semiconductors using a plane-wave basis set, Comput. Mater. Sci. 6 (1996) 15–50.

[27] G. Kresse, J. Furthmüller, Efficient iterative schemes for ab initio total-energy calculations using a plane-wave basis set, Phys. Rev. B 54 (1996) 11169–11186.

[28] G. Kresse, D. Joubert, From ultrasoft pseudopotentials to the projector augmented-wave method, Phys. Rev. B. 59 (1999) 1758–1775.

[29] L. Chen, C. Zhang, Y. Li, C.-R. Chang, C. He, Q. Lu, Y. Yu, P. Duan, Z. Zhang, R. Luque, Hierarchically hollow MnO₂@CeO₂ heterostructures for NO oxidation: remarkably promoted activity and SO₂ tolerance, ACS Catal. 11 (2021) 10988–10996.

[30] Y. Xin, L. Cheng, Y. Lv, J. Jia, D. Han, N. Zhang, J. Wang, Z. Zhang, X.-M. Cao, Experimental and theoretical insight into the facet-dependent mechanisms of NO oxidation catalyzed by structurally diverse Mn₂O₃ nanocrystals, ACS Catal. (2021) 397–410.

[31] K. Khaledi, M. Haghighi, P. Sadeghpour, On the catalytic properties and performance of core-shell ZSM-5@MnO nanocatalyst used in conversion of methanol to light olefins, Microporous Mesoporous Mater. 246 (2017) 51–61.

[32] Z. Liu, Z. Wu, X. Peng, A. Binder, S. Chai, S. Dai, Origin of active oxygen in a ternary CuOₓ/Co₃O₄–CeO₂ catalyst for CO oxidation, J. Phys. Chem. C 118 (2014) 27870–27877.

[33] L. Chen, J. Zhang, Y. Li, X. Wu, Z. Zhang, Q. Lu, C. He, Taming NO oxidation efficiency by γ-MnO₂ morphology regulation, Catal. Sci. Technol. 10 (2020) 5996–6005.

[34] Z. Li, S. Dai, L. Ma, Z. Qu, N. Yan, J. Li, Synergistic interaction and mechanistic evaluation of NO oxidation catalysis on Pt/Fe₂O₃ cubes, Chem. Eng. J. 413 (2021), 127447.

[35] P.H. Ho, J.-W. Woo, R. Feizie Ilmasani, J. Han, L. Olsson, The role of Pd–Pt Interactions in the oxidation and sulfur resistance of bimetallic Pd–Pt/γ-Al₂O₃ diesel oxidation catalysts, Ind. Eng. Chem. Res. 60 (2021) 6596–6612.

[36] J. Hwang, R.R. Rao, L. Giordano, K. Akkiraju, X.R. Wang, E.J. Crumlin, H. Bluhm, Y. Shao-Horn, Regulating oxygen activity of perovskites to promote NOₓ oxidation and reduction kinetics, Nat. Catal. 4 (2021) 663–673.

[37] T. Zhang, H. Li, Z. Yang, F. Cao, L. Li, H. Chen, H. Liu, K. Xiong, J. Wu, Z. Hong, W. Wang, Electrospun YMn₂O₅ nanofibers: a highly catalytic activity for NO oxidation, Appl. Catal. B 247 (2019) 133–141.

[38] K. Yu, D. Lei, Y. Feng, H. Yu, Y. Chang, Y. Wang, Y. Liu, G.-C. Wang, L.-L. Lou, S. Liu, W. Zhou, The role of Bi-doping in promoting electron transfer and catalytic performance of Pt/3DOM-Ce₁₋ₓBixO₂₋δ, J. Catal. 365 (2018) 292–302.

[39] M.A. Henderson, C.L. Perkins, M.H. Engelhard, S. Thevuthasan, C.H.F. Peden, Redox properties of water on the oxidized and reduced surfaces of CeO₂(111), Surf. Sci. 526 (2003) 1–18.

[40] H. Yan, Q. Shen, Y. Sun, S. Zhao, R. Lu, M. Gong, C. Yang, Tailoring facets of α-Mn₂O₃ microcrystalline catalysts for enhanced selective oxidation of glycerol to glycolic acid, ACS Catal. 11 (2021) 6371–6383.

[41] W. Yang, H. Huang, X. Ding, Z. Ding, C. Wu, I.D. Gates, Z. Gao, Theoretical study on double-atom catalysts supported with graphene for electroreduction of nitrogen into ammonia, Electrochim. Acta 335 (2020), 135667.

[42] C. Song, Q. Zhan, F. Liu, C. Wang, H. Li, X. Wang, X. Guo, Y. Cheng, W. Sun, L. Wang, J. Qian, B. Pan, Overturned loading of inert CeO₂ to active Co₃O₄ for unusually improved catalytic activity in Fenton-like reactions, Angew. Chem. Int. Ed. (2022), e202200406.

[43] Y.-F. Han, K. Ramesh, L. Chen, E. Widjaja, S. Chilukoti, F. Chen, Observation of the reversible phase-transformation of α-Mn₂O₃ nanocrystals during the catalytic combustion of methane by in situ raman spectroscopy, J. Phys. Chem. C 111 (2007) 2830–2833.

[44] J. Xu, Y.-Q. Deng, Y. Luo, W. Mao, X.-J. Yang, Y.-F. Han, Operando raman spectroscopy and kinetic study of low-temperature CO oxidation on an α-Mn₂O₃ nanocatalyst, J. Catal. 300 (2013) 225–234.

[45] Y. Shen, J. Deng, L. Han, W. Ren, D. Zhang, Low-temperature combustion of toluene over Cu-doped SmMn₂O₅ mullite catalysts via creating highly active Cu²⁺–O–Mn⁴⁺ sites, Environ. Sci. Technol. 56 (2022) 10433–10441.

[46] L. Li, C. Zhang, J. Yan, D. Wang, Y. Peng, J. Li, J. Crittenden, Distinctive bimetallic oxides for enhanced catalytic toluene combustion: insights into the tunable fabrication of Mn–Ce hollow structure, ChemCatChem 12 (2020) 2872–2879.

[47] S. Rong, P. Zhang, F. Liu, Y. Yang, Engineering crystal facet of α-MnO₂ nanowire for highly efficient catalytic oxidation of carcinogenic airborne formaldehyde, ACS Catal. 8 (2018) 3435–3446.

[48] J. Ma, G. Jin, X. Gao, Y. Li, L. Dong, M. Huang, Q. Huang, B. Li, Catalytic effect of two-phase intergrowth and coexistence CuO–CeO₂, J. Mater. Chem. 3 (2015) 24358–24370.

[49] S. Xiong, J. Chen, N. Huang, T. Yan, Y. Peng, J. Li, The poisoning mechanism of gaseous HCl on low-temperature SCR catalysts: MnOₓ–CeO₂ as an example, Appl. Catal. B 267 (2020), 118668.

[50] L.A.J. Garvie, P.R. Buseck, Determination of Ce⁴⁺/Ce³⁺ in electron-beam-damaged CeO₂ by electron energy-loss spectroscopy, J. Phys. Chem. Solids 60 (1999) 1943–1947.

[51] Y. Pei, Q. Chen, M. Wang, B. Li, P. Wang, G. Henkelman, L. Zhen, G. Cao, C.-Y. Xu, Reviving reversible anion redox in 3d-transition-metal Li rich oxides by introducing surface defects, Nano Energy 71 (2020), 104644.

[52] L. He, Y. Zhang, Y. Zang, C. Liu, W. Wang, R. Han, N. Ji, S. Zhang, Q. Liu, Promotion of A-site Ag-doped perovskites for the catalytic oxidation of soot: synergistic catalytic effect of dual active sites, ACS Catal. 11 (2021) 14224–14236.

[53] X. Yao, L. Chen, J. Cao, Y. Chen, M. Tian, F. Yang, J. Sun, C. Tang, L. Dong, Enhancing the deNOₓ performance of MnOx/CeO₂-ZrO₂ nanorod catalyst for low-temperature NH₃-SCR by TiO₂ modification, Chem. Eng. J. 369 (2019) 46–56.

[54] Y. Peng, K. Li, J. Li, Identification of the active sites on CeO$_2$–WO$_3$ catalysts for SCR of NO$_x$ with NH$_3$: an in situ IR and raman spectroscopy study, Appl. Catal. B 1140-141 (2013) 483–492.

[55] B. Qin, R.T. Guo, J. Zhou, L.G. Wei, T.Y. Yin, W.G. Pan, A novel flower-like MnCe/TiO$_2$ catalyst with controlled morphology for low-temperature selective catalytic reduction of NO with NH$_3$, Appl. Surf. Sci. 598 (2022), 153823.

[56] X. Wang, Y. Liu, Z. Wu, The poisoning mechanisms of different zinc species on a ceria-based NH$_3$-SCR catalyst and the co-effects of zinc and gas-phase sulfur/chlorine species, J. Colloid Interface Sci. 566 (2020) 153–162.

[57] C. Wang, F. Gao, S. Ko, H. Liu, H. Yi, X. Tang, Structural control for inhibiting SO$_2$ adsorption in porous MnCe nanowire aerogel catalysts for low-temperature NH$_3$-SCR, Chem. Eng. J. 434 (2022), 134729.